Journal of Cluster Science
https://doi.org/10.1007/s10876-020-01943-z

ORIGINAL PAPER

Axially Chiral Cage-Like B_{38}^{+} and B_{38}^{2+}: New Aromatic Members of the Borospherene Family

Hui Liu[1] · Yue-Wen Mu[1] · Si-Dian Li[1]

Received: 2 March 2020 / Accepted: 9 November 2020

Abstract
The successive discoveries of the cage-like D_{2d} $B_{40}^{-/0}$ and C_3/C_2 B_{39}^{-} mark the onset of borospherene chemistry. Based on extensive global minimum searches and first-principles theory calculations, we predict herein the possible existence of the axially chiral cage-like C_2 B_{38}^{+} (**1**/**1′**) and C_2 B_{38}^{2+} (**3**/**3′**) which are novel aromatic members of the borospherene family featuring a B_{21} boron triple-chain on the waist and four B_6 hexagonal holes on the cage surface. Detailed bonding analyses show that the B_{38}^{+} (**1**) and B_{38}^{2+} (**3**) possess 12 and 11 delocalized π bonds over a σ-skeleton, respectively, following the universal bonding pattern of σ + π double delocalization of the borospherene family. Extensive molecular dynamics simulations indicate that both B_{38}^{+} (**1**) and B_{38}^{2+} (**3**) are dynamically stable at 700 K. The IR, Raman, and UV–vis spectra of these cluster cations are computationally simulated to facilitate their future spectral characterizations.

Keywords First-principles theory · Boron clusters · Borospherenes · Structures · Bonding

Introduction

As prototypical electron-deficient element in the periodical table, boron exhibits strong propensity to form delocalized multicenter-two-electron (mc-2e) bonds in both bulk allotropes and polyhedral molecules [1–3]. Over the past two decades, anionic boron clusters B_n^{-} (n = 3–38,41,42) have been systematically confirmed to possess planar or quasi-planar (2D) global minimum (GM) structures via joint photoelectron spectroscopy (PES) and extensive first-principles theory investigations [4–16]. 2D B_n^{-} clusters featuring both delocalized mc-2e σ and π bonds are composed of B_3 triangular networks with certain numbers of polygonal holes. After the discovery of the perfect quasi-planar $B_{36}^{-/0}$ cluster with a hexagonal hole at the center in 2014, [14] more 2D boron clusters with a double hexagonal vacancy (DHV) were observed, including B_{35}^{-}, B_{37}^{-}, B_{38}^{-}, [13, 15] and the more recently reported B_{41}^{-} and B_{42}^{-} clusters [16], providing indirect evidence for the existence of 2D all-boron sheets dubbed borophenes with various hexagonal vacancy densities. [14, 17, 18] Supported polymorphous borophenes on various metal substrates were prepared using molecular beam epitaxy (MBE) method [19–22].

A major breakthrough in the studies of boron clusters occurred in 2014 when the first all-boron fullerenes D_{2d} $B_{40}^{-/0}$, dubbed borospherenes [23] were discovered in a joint PES and theoretical investigation. $B_{40}^{-/0}$ are found to be composed of twelve interwoven boron double-chains (BDCs) [24, 25] with two hexagon holes on the top and bottom and four heptagon holes on the waist. Shortly after, the first axially chiral borospherenes C_3/C_2 B_{39}^{-} were observed experimentally as the GMs of the monoanion [26]. Cage-like B_{42}^{2+}, B_{41}^{+}, B_{38}^{2-}, B_{37}^{3-}, and B_{36}^{4-} clusters in different charge states were late predicted by our group at first-principles theory level [27–30]. These medium-sized cage-like B_n^{q} (n = 36–42, q = n-40) boron clusters form a borospherene family which are all composed of twelve interwoven BDCs with six hexagonal or heptagonal facets and follow the universal bonding pattern

Electronic supplementary material The online version of this article (https://doi.org/10.1007/s10876-020-01943-z) contains supplementary material, which is available to authorized users.

✉ Yue-Wen Mu
ywmu@sxu.edu.cn

✉ Si-Dian Li
lisidian@sxu.edu.cn

[1] Nanocluster Laboratory, Institute of Molecular Science, Shanxi University, Taiyuan 030006, Shanxi, People's Republic of China

Published online: 23 November 2020

of σ + π double delocalization. Meanwhile, seashell-like C_2 $B_{28}^{-/0}$ and C_s B_{29}^- borospherenes were observed for smaller B_n clusters in PES measurements as minor isomers of the systems [9]. Our group later predicted the possibility of seashell-like C_s B_{29}^+, C_2 B_{31}^+, C_2 B_{32}, C_2 B_{34}, and C_2 B_{35}^+ in theory [31–33]. They all appear to follow the universal σ + π double delocalization bonding pattern of the borospherene family. For the cationic B_n^+ clusters (n = 16 ~ 25), the transition from two-dimensional to double-ring structures occurs at B_{16}^+ in ion-mobility measurements [34]. A high-symmetry cage-like D_{2h} B_{38} neutral with four hexagonal holes on the surface was predicted as the GM of B_{38} at density functional theory (DFT) level in 2014 [35]. However, there has been no experimental evidence available to confirm this perfect D_{2h} neutral structure to date. Neither experimental nor theoretical studies have been reported on B_{38}^+ monocation or B_{38}^{2+} dication to probe the charge-induced structural changes in B_{38}.

Based on extensive GM searches and first-principles theory calculations, we predict herein the possibility of the axially chiral cage-like C_2 B_{38}^+ (**1/1′**) and C_2 B_{38}^{2+} (**3/3′**) which are new aromatic members of the borospherene family. Both B_{38}^+(**1**) and B_{38}^{2+}(**3**) feature a B_{21} boron triple-chain on the waist and four B_6 hexagonal holes on the surface and follow the universal σ + π double delocalization bonding pattern of borospherene clusters.

Theoretical Methods

Extensive GM structural searches were performed on B_{38}^+ and B_{38}^{2+} using the TGmin 2.0 package, [36–38] in combination with manual structural constructions based on the previously reported low-lying cage-like, tubular, or quasi-planar isomers of B_{38}, B_{38}^-, B_{39}^- and B_{39}^+ clusters [15, 26, 35, 39]. In total, about 7600 and 7000 trial isomers were probed using the TGMin approach for B_{38}^+ and B_{38}^{2+}, respectively. Full geometry optimizations and frequency analyses of the obtained low-lying isomers of the B_{38}^+ and B_{38}^{2+} were performed at DFT-PBE0 [40] level with the basis set of 6-311 + G(d) [41] using Gaussian 09 suite. [42] To obtain more accurate relative energies, single point electronic energies of the five lowest-lying isomers were calculated at the PBE0 geometries using the more accurate coupled cluster CCSD(T) method [43–45] with the 6-31G(d) basis set implemented in MOLPRO 2012 [46]. The optimized borospherenes C_2 B_{38}^+ (**1/1′**, ^{2}A), D_{2h} B_{38}^+ (**2**, $^2B_{3u}$), C_2 B_{38}^{2+} (**3/3′**, ^{1}A), and D_{2h} B_{38}^{2+} (**4**, ^1A_g) are depicted in Fig. 1. More alternative low-lying isomers are comparatively depicted in Fig. 2, Fig.S1, and Fig.S2 (ESI†). Detailed bonding pattern analyses were performed on C_2 B_{38}, D_{2h} B_{38}, and C_2 B_{38}^{2+} using the adaptive

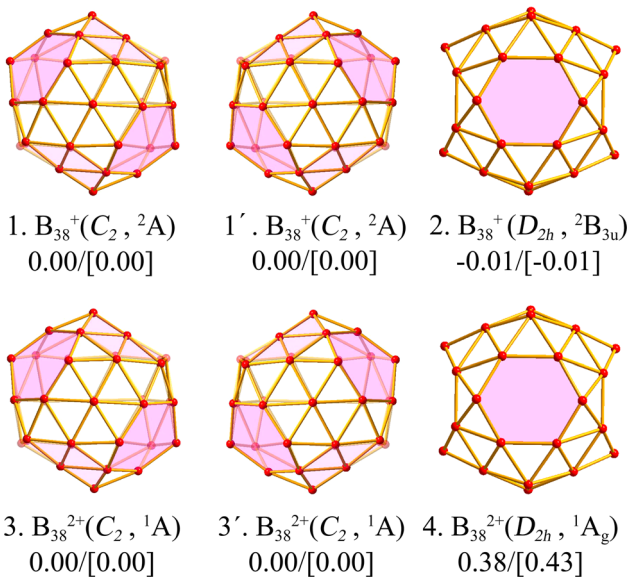

Fig. 1 Optimized structures of the axially chiral cage-like C_2 B_{38}^+ (**1/1′**) and C_2 B_{38}^{2+} (**3/3′**) in comparison with that of D_{2h} B_{38}^+ (**2**) and D_{2h} B_{38}^{2+} (**4**), with the relative energies indicated in eV at the PBE0/6-311 + G(d) and CCSD(T)/6-31G(d) (in square brackets) levels. The B_6 heptagonal holes on the cage surfaces are highlighted in pink (Color figure online)

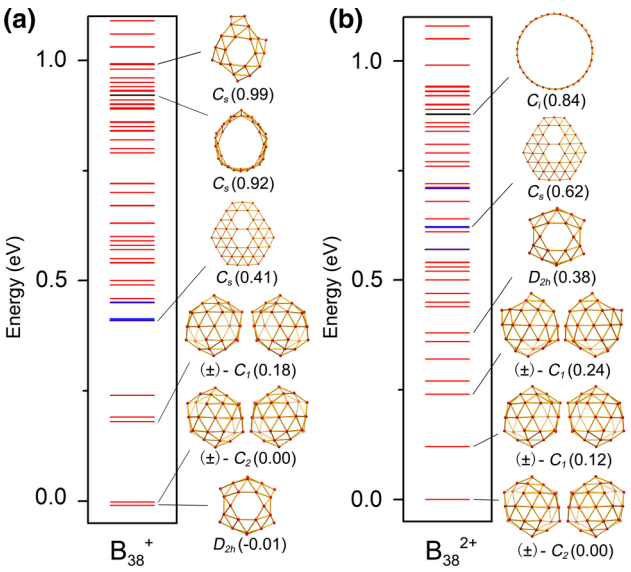

Fig. 2 Configurational energy spectra of **a** B_{38}^+ and **b** B_{38}^{2+} at PBE0/6-311 + G* level. The energy of the global minimum is taken to be zero and the relative energies are in eV. The red, blue and black bars denote fullerene-like cages, quasi-planar, and triple-ring tubular structures, respectively (Color figure online)

natural density partitioning (AdNDP) approach to recover both the localized and delocalized bonds of the concerned systems [47]. Nucleus-independent chemical shifts (NICS) [48] were calculated at the centers of the cage-like C_2 B_{38}^+ (**1**) and C_2 B_{38}^{2+} (**3**) to assess their spherical aromaticities. Born–Oppenheimer molecular dynamics (MD) simulations were performed on C_2 B_{38}^+ (**1**) and C_2 B_{38}^{2+} (**3**) at

different temperatures for 30 ps to investigate their dynamic stabilities using the CP2K software. [49]

Results and Discussion

Structures and Stabilities

We start from the open-shell B_{38}^{+} monocation by detaching one valence electron from previously reported neutral B_{38} which has a perfect D_{2h} GM [35]. As shown in Fig. 1, the newly obtained axially chiral cage-like C_2 B_{38}^{+} (1, ^{2}A) and its degenerate enantiomer C_2 B_{38}^{+} (**1́**, ^{2}A) with the HOMO–LUMO gaps of $\Delta E_{gap(\alpha)}$ = 1.72 eV and $\Delta E_{gap(\beta)}$ = 1.65 eV feature a B_{21} boron triple-chain on the waist at the back and four B_6 hexagons on the top and bottom in an overall C_2 symmetry, similar to the previously reported C_2 B_{34} and C_2 B_{35}^{+}. [41] They follow Euler's rule in this case which reads: E (96 edges) = F (56 triangular + 4 hexagonal faces) + V (38 vertices) − 2. More interestingly, as shown in Fig. 2a, with the small energy difference of 0.01 eV at both PBE0 and UCCSD(T) levels, C_2 (**1/1′**) can be practically viewed as iso-energetic isomers of the perfect cage-like D_{2h} B_{38}^{+} (**2**) with $\Delta E_{gap(\alpha)}$ = 2.29 eV and $\Delta E_{gap(\beta)}$ = 1.80 eV. These cage-like configurational isomers with four B_6 hexagonal holes on the surface may therefore coexist in experiments in gas phases. The third lowest-lying chiral cage-like C_1 B_{38}^{+} which is also a configurational isomer of C_2 B_{38}^{+} (**1/1′**) and D_{2h} B_{38}^{+} (**2**) with four B_6 hexagons on the surface possesses the relative energy of 0.18 eV at both PBE0 and UCCSD(T) (Fig. 2a and Fig.S1). In fact, as shown in Fig. 2a, most of the low-lying B_{38}^{+} isomers within 1 eV above the GM possess cage-like structures, whereas the first quasi-planar isomer C_s B_{38}^{+} with a DHV which has the same geometry as the experimentally observed C_s B_{38}^{-} [15] turns out to lie 0.35 eV higher than C_2 B_{38}^{+} (**1**) at the most accurate CCSD(T) level. The cage-like C_s B_{38}^{+} with the same geometry as the theoretically predicted C_s GM of B_{38}^{2-} [28] appears to have the relative energy of 0.99 eV at PBE0. The axially chiral C_2 B_{38}^{+} (**1/1′**) and D_{2h} B_{38}^{+} (2) are therefore the lowest-lying isomers of the B_{38}^{+} possible to be observed in experiments.

As shown in Figs. 2b and S2, with one more electron detached from the monocation, the closed-shell axially chiral dications C_2 B_{38}^{2+} (**3/3′**, ^{1}A) with ΔE_{gap} = 1.81 eV turned to be 0.38 eV and 0.43 eV more stable than the seventh lowest-lying isomer D_{2h} B_{38}^{2+} (**4**) with ΔE_{gap} = 1.83 eV at PBE0 and CCSD(T) levels, respectively, indicating that B_{38}^{2+} dication exhibits an obvious charged-induced structural change for which the axially chiral C_2 B_{38}^{2+} (**3/3′**) become obviously GMs of the system. The second and third lowest-lying cage-like C_1 B_{38}^{2+} and C_1 B_{38}^{2+} with four B_6 hexagons on the cage surface have the relative energies of 0.10 eV and 0.19 eV at PBE0 and 0.10 eV and 0.19 eV at CCSD(T), respectively. The fourth isomer C_{2h} B_{38}^{2+} which has two tetracoordinate ''defect sites'' on the waist, similar to the experimentally observed C_2 B_{39}^{-} and the theoretically predicted C_2 B_{34}, [26, 32] turns out to lie 0.21 eV higher than the GM C_2 (**3**) at CCSD(T). The typical quasi-planar C_s B_{38}^{2+} in the same geometry as the experimentally observed B_{38}^{-} has the relative energy of 0.62 eV at PBE0 (Fig.S2).

Extensive MD simulations in Fig. 3 and Fig. S3 indicate that both C_2 B_{38}^{+} (**1**) and C_2 B_{38}^{+} (**3**) are dynamically stable at 700 K, with the average root-mean-square-deviations of RMSD = 0.08 and 0.09 Å and maximum bond length deviations of MAXD = 0.26 and 0.29 Å, respectively. However, at 900 K, B_{38}^{+} (**1**) starts to fluctuate between two low-lying cage-like isomers ($C_2 \leftrightarrow C_1$) in a concerned W-X-M transformation mechanism [50] with RMSD = 0.14 Å and MAXD = 0.65 Å. Similar situation happens in C_2 B_{38}^{2+} (**3**) dication which also exhibits a $C_2 \leftrightarrow C_1$ structural fluctuation at 900 K (Fig. S3).

Bonding Pattern Analyses

To better understand the high stability of the open-shell C_2 B_{38}^{+} (**1**) monocation, we chose to analyze the AdNdP bonding pattern of the closed-shell C_2 B_{38} neutral which has a fully occupied highest occupied molecular orbital (HOMO). As shown in Fig. 4a, C_2 B_{38} possesses 36 3c-2e σ bonds, 8 4c-2e σ bonds, and 1 7c-2e σ bond with the occupation numbers between ON = 1.78–1.96 lel, forming

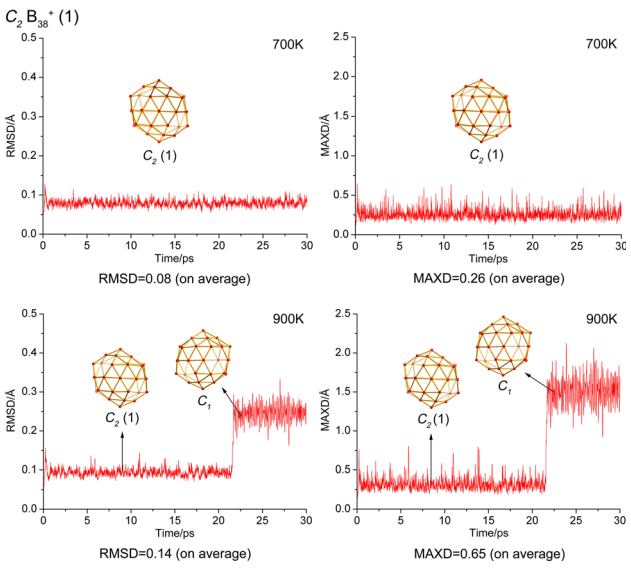

Fig. 3 Born–Oppenheimer molecular dynamics simulations of C_2 B_{38}^{+} (**1**) at 700 K and 900 K, with the calculated average root-mean-square-deviation (RMSD) and maximum bond length deviation (MAXD) values indicated in Å

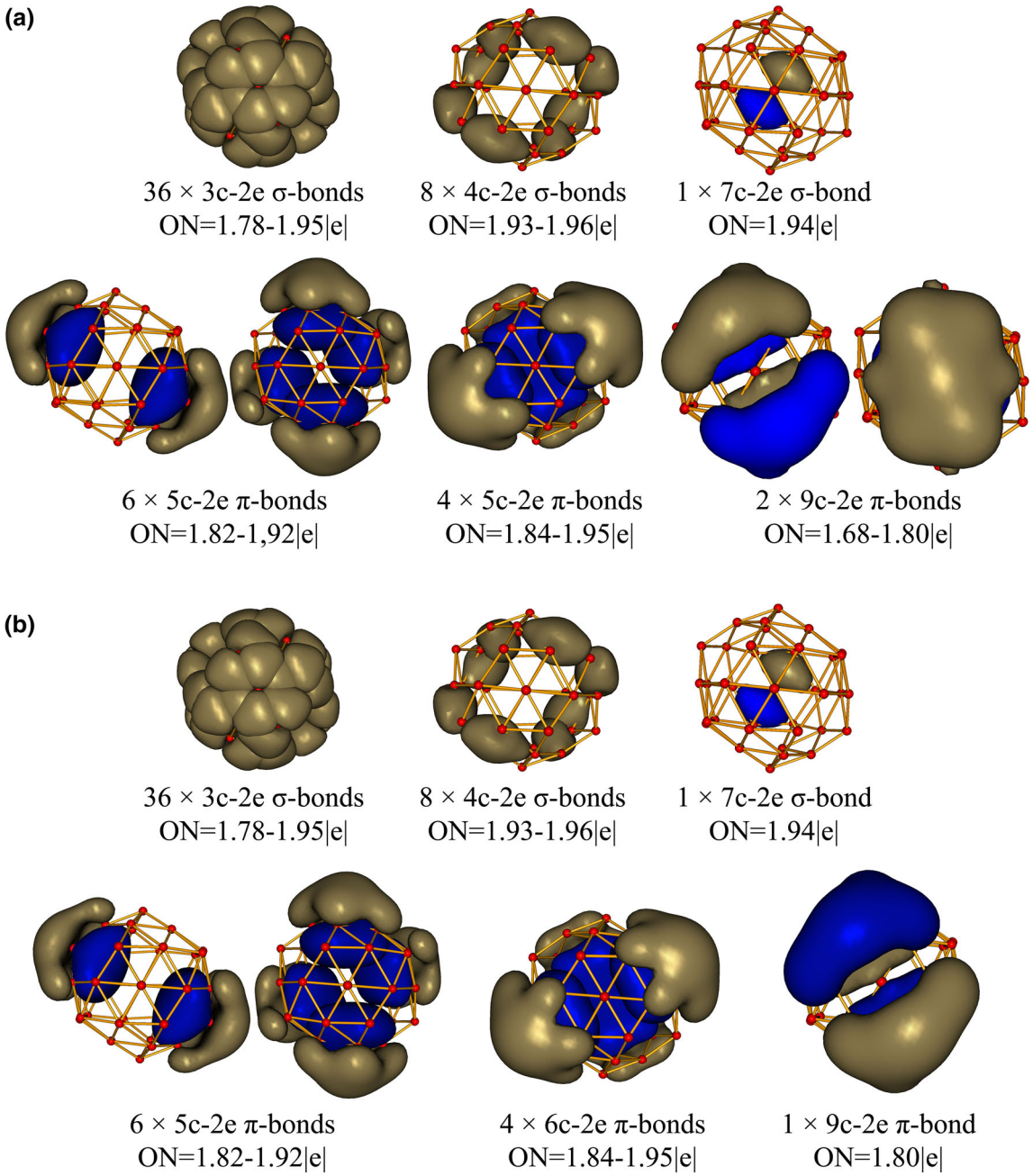

Fig. 4 AdNDP bonding patterns of the closed-shell **a** C_2 B_{38} and **b** C_2 B_{38}^{2+}(**3**), with the occupation numbers (ONs) indicated

the σ-skeleton on the cage surface. The remaining 24 valence electrons form 12 delocalized π bonds over the cage surface, including 6 5c-2e π bonds on the top and bottom with ON = 1.82–1.92 |e|, 4 5c-2e π bonds on the waist with ON = 1.84–1.95 |e|, and 2 9c-2e π bonds in the front of the cage with ON = 1.68–1.80 |e|, in an overall symmetry of C_2. These delocalized π-bonds originate from the 12 totally delocalized molecular orbitals of C_2 B_{38} depicted in Fig.S5a. The open-shell C_2 B_{38}^{+} (**1**) monocation which has one less valence electron than the C_2 neutral also has 12 delocalized π bonds, with the second 9c-2e π bond in the front of the cage singly occupied. Similar to C_2 B_{38}, the previously reported neutral D_{2h} B_{38} (**2**) possesses 12 delocalized π bonds over an σ-skeleton (Fig. S4).

With one more valence electron detached from the HOMO of C_2 B_{38}, C_2 B_{38}^{2+} (**3**) dication possesses 11 delocalized π bonds (6 5c-2e, 4 5c-2e, and 1 9c-2e π) over the same σ-skeleton as in the neutral (Fig. 4b), with the second 9c-2e π bond in the front of the cage emptied, in line with the 11 totally delocalized CMOs of C_2 B_{38}^{2+}

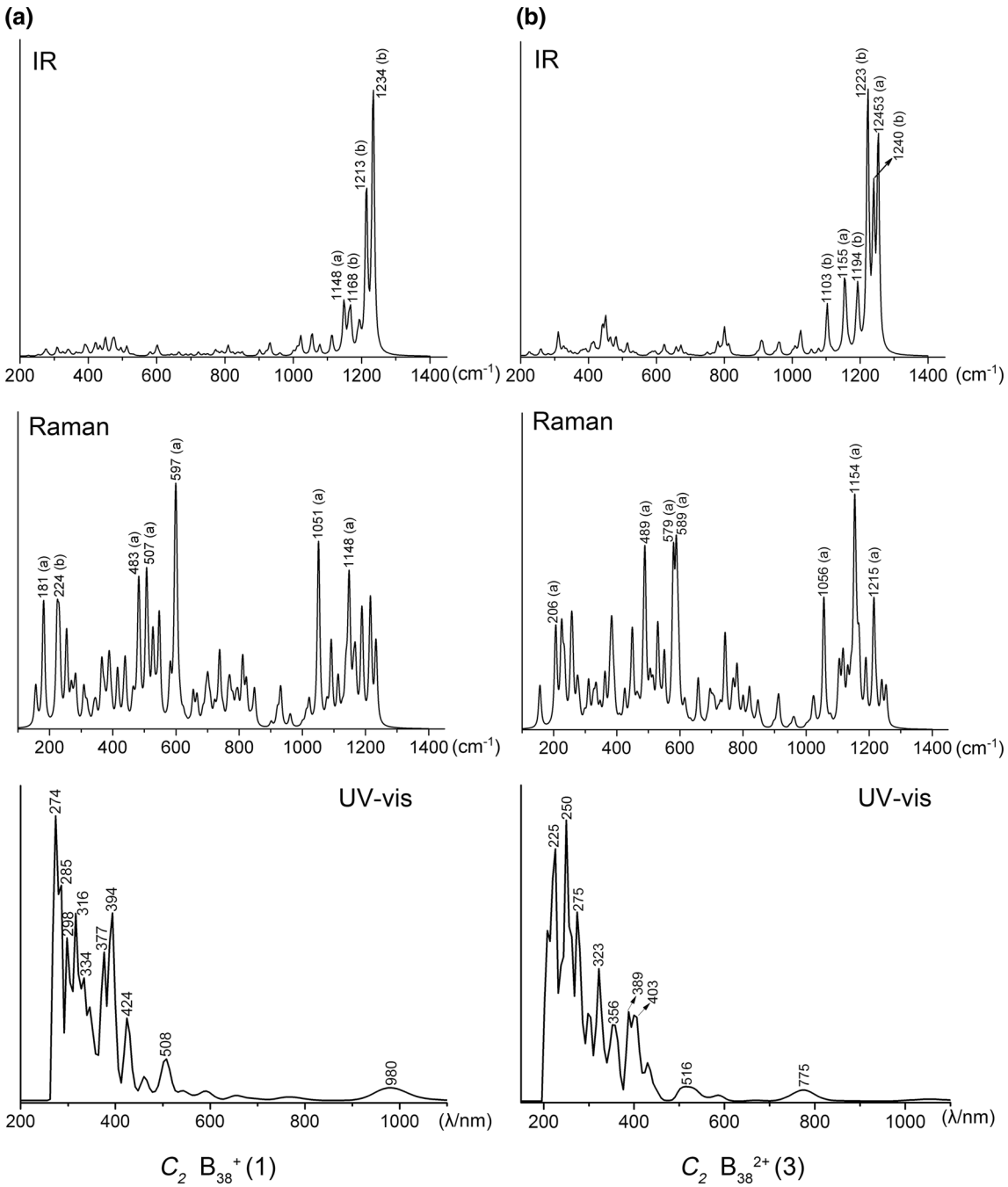

Fig. 5 Simulated IR, Raman, and UV–vis spectra of **a** C_2 B_{38}^{+} (**1**) and **b** C_2 B_{38}^{2+} (**3**) at the PBE0/6-311 + G(d) level

shown in Fig.S5b. Such a π-bonding pattern helps to stabilize C_2 B_{38}^{2+} (**3**) effectively, making it the obvious GM of the dication (Fig. 2b). According to the bonding patterns obtained above, both C_{2h} B_{38}^{+} (**1**) and C_2 B_{38}^{2+} (**3**) follow the universal σ + π double delocalization bonding pattern of the borospherene family. These axially chiral clusters appear to be spherically aromatic in nature, as evidenced by their calculated negative NICS values of − 18 ppm and − 10 ppm at the cage centers at PBE0/6-311 + G(d) level, respectively. Similar situations happen in the experimentally observed spherically aromatic D_{2d} B_{40} and C_3/C_2 B_{39}^{-} which each possess 12 delocalized π bonds [23–25].

Spectral Simulations

The simulated infrared (IR) spectra of C_2 B_{38}^{+} (**1**) and C_2 B_{38}^{2+} (**3**) at PBE0/6-311 + G(d) appear to be similar (Fig. 5), with the major IR active peaks at 1148 cm^{-1} (b), 1213 cm^{-1} (b), and 1234 cm^{-1} (b) in C_2 B_{38}^{+} (**1**) and at

1223 cm^{-1} (b), 1240 cm^{-1} (b), and 1253 cm^{-1} (a) in C_2 B_{38}^{2+} (3), respectively. Other IR active vibrational modes turn out to have much lower intensities.

The simulated Raman spectra of C_2 B_{38}^{+} (**1**) and C_2 B_{38}^{2+} (**3**) possess the major Raman active peaks at 597 cm^{-1} (a), 1051 cm^{-1} (a), and 1148 cm^{-1} (a) in the former and at 489 cm^{-1} (b), 579 cm^{-1} (a), 589 cm^{-1} (a), and 1154 cm^{-1} (a) in the latter. Among the Raman active modes, the vibrations at 181 cm^{-1} (a) in B_{38}^{+} (**1**) and 206 cm^{-1} (a) in B_{38}^{2+} (**3**) belong to typical "radial breathing modes" (RBMs) of the two borospherenes. Similar RBM vibrations have been used to characterize the hollow structures in single-walled boron nanotubes. [51]

Finally, we present the simulated UV–vis spectra of C_2 B_{38}^{+} (**1**) and C_2 B_{38}^{2+} (**3**) using the time-dependent (TD) DFT approach [52] at PBE0/6-311 + G(d) level. The main UV absorptions of these borospherenes occur at 274 nm, 298 nm, 316 nm, and 394 nm in C_2 B_{38}^{+} (**1**), and 250 nm, 323 nm, and 389 nm in C_2 B_{38}^{2+} (**3**). The weak UV–vis absorptions bands at 980 nm in C_2 B_{38}^{+} (**1**) and 775 nm in C_2 B_{38}^{2+} (**3**) originate from HOMO-4 → SOMO and HOMO-3 → LUMO excitations, respectively.

Conclusions

In summary, we have performed a detailed theoretical investigation on B_{38}^{+} monocation and B_{38}^{2+} dication and presented two new axially chiral aromatic members C_2 B_{38}^{+} (**1**/**1′**) and C_2 B_{38}^{2+} (**3**/**3′**) to the borospherene family in this work. These novel borospherenes feature one B_{21} triple-ring chain on the waist and four B_6 hexagonal holes on the cage surface and follow the universal σ + π double delocalization bonding pattern of the borospherene family. The simulated IR, Raman and UV–Vis spectra may help facilitate their future spectral characterizations in gas phases. Theoretical investigations on cage-like borospherenes provide valuable information on their experimental syntheses and potential applications as novel boron nanomaterials.

Acknowledgements The project was financially supported by the National Natural Science Foundation of China (21720102006 and 21973057 to S.-D. Li).

Compliance with Ethical Standards

Conflict of interest There are no conflicts to declare.

References

1. F. A. Cotton, G. Wilkinson, C. A. Murillo, and M. Bochmann (1999). *Adv. Inorg. Chem.* **131**, 1376.
2. M. Fujimori, T. Nakata, T. Nakayama, E. Nishibori, K. Kimura, M. Takata, and M. Sakata (1999). *Phys. Rev. Lett.* **82**, 4452–4455.
3. A. R. Oganov, J. Chen, C. Gatti, Y. Ma, Y. Ma, C. W. Glass, Z. Liu, T. Yu, O. O. Kurakevych, and V. L. Solozhenko (2009). *Nature.* **457**, 863.
4. A. N. Alexandrova, A. I. Boldyrev, H. J. Zhai, and L. S. Wang (2006). *Coord. Chem. Rev.* **250**, 2811.
5. A. P. Sergeeva, I. A. Popov, Z. A. Piazza, W. L. Li, C. Romanescu, L. S. Wang, and A. I. Boldyrev (2014). *Acc. Chem. Res.* **47**, 1349–1358.
6. L. S. Wang (2016). *Int. Rev. Phys. Chem.* **35**, 69–142.
7. X. M. Luo, T. Jian, L. J. Cheng, W. L. Li, Q. Chen, R. Li, H. J. Zhai, S. D. Li, A. I. Boldyrev, J. Li, and L. S. Wang (2017). *Chem. Phys. Lett.* **683**, 336–341.
8. Y. J. Wang, Y. F. Zhao, W. L. Li, T. Jian, Q. Chen, X. R. You, T. Ou, X. Y. Zhao, H. J. Zhai, S. D. Li, J. Li, and L. S. Wang (2016). *J. Chem. Phys.* **144**, 064307.
9. H. R. Li, T. Jian, W. L. Li, Ch. Q. Miao, Y. J. Wang, Q. Chen, X. M. Luo, K. Wang, H. J. Zhai, S. D. Li, and L. S. Wang (2016). *Phys. Chem. Chem. Phys.* **18**, 29147–29155.
10. W. L. Li, Y. F. Zhao, H. S. Hu, J. Li, and L. S. Wang (2014). *Angew. Chem. Int. Ed.* **53**, 5540–5545.
11. Q. Chen, T. T. Chen, H. R. Li, X. Y. Zhao, W. J. Chen, H. J. Zhai, S. D. Li, and L. S. Wang (2019). *Nanoscale.* **11**, 9698–9704.
12. Q. Chen, W. L. Li, X. Y. Zhao, H. R. Li, L. Y. Feng, H. J. Zhai, S. D. Li, and L. S. Wang (2017). *Eur. J. Inorg. Chem.* **38**, 4546–4551.
13. W. L. Li, Q. Chen, W. J. Tian, H. Bai, Y. F. Zhao, H. S. Hu, J. Li, H. J. Zhai, S. D. Li, and L. S. Wang (2014). *J. Am. Chem. Soc.* **136**, 12257–12260.
14. Z. A. Piazza, H. S. Hu, W. L. Li, Y. F. Zhao, J. Li, and L. S. Wang (2014). *Nat. Commun.* **5**, 3113.
15. Q. Chen, W. J. Tian, L. Y. Feng, H. G. Lu, Y. W. Mu, H. J. Zhai, S. D. Li, and L. S. Wang (2017). *Nanoscale.* **9**, 4550–4557.
16. H. Bai, T. T. Chen, Q. Chen, X. Y. Zhao, Y. Y. Zhang, W. J. Chen, W. L. Li, L. F. Cheung, B. Bai, J. Cavanagh, W. Huang, S. D. Li, J. Li, and L. S. Wang (2019). *Nanoscale.* **11**, 23286–23295.
17. Z. Zhang, A. J. Mannix, Z. Hu, B. Kiraly, N. P. Guisinger, M. C. Hersam, and B. I. Yakobson (2016). *Nano Lett.* **16**, 6622.
18. Z. Zhang, Y. Yang, G. Y. Gao, and B. I. Yakobson (2015). *Angew. Chem. Int. Ed.* **54**, 13022–13026.
19. A. J. Mannix, X. F. Zhou, B. Kiraly, J. D. Wood, D. Alducin, B. D. Myers, X. Liu, B. L. Fisher, U. Santiago, J. R. Guest, M. J. Yacaman, A. Ponce, A. R. Oganov, M. C. Hersam, and N. P. Guisinger (2015). *Science.* **350**, 1513.
20. B. Feng, J. Zhang, Q. Zhong, W. Li, S. Li, H. Li, P. Cheng, S. Meng, L. Chen, and K. Wu (2016). *Nat. Chem.* **8**, 563.
21. R. Wu, I. K. Drozdov, S. Eltinge, P. Zahl, S. Ismail-Beigi, I. Božović, and A. Gozar (2019). *Nature Nanotechol.* **14**, 44–49.
22. B. Kiraly, X. L. Liu, L. Q. Wang, Z. Zhang, A. J. Mannix, B. L. Fisher, B. I. Yakobson, M. C. Hersam, and N. P. Guisinger (2019). *ACS Nano.* **13**, 3816–3822.
23. H. J. Zhai, Y. F. Zhao, W. L. Li, Q. Chen, H. Bai, H. S. Hu, Z. A. Piazza, W. J. Tian, H. G. Lu, Y. B. Wu, Y. W. Mu, G. F. Wei, Z. P. Liu, J. Li, S. D. Li, and L. S. Wang (2014). *Nat. Chem.* **6**, 727–731.
24. W. L. Li, C. Romanescu, T. Jian, and L. S. Wang (2012). *J. Am. Chem. Soc.* **134**, 13228–13231.

25. D. Z. Li, Q. Chen, Y. B. Wu, H. G. Lu, and S. D. Li (2012). *Phys. Chem. Chem. Phys.* **14**, 14769–14774.
26. Q. Chen, W. L. Li, Y. F. Zhao, S. Y. Zhang, H. S. Hu, H. Bai, H. R. Li, W. J. Tian, H. G. Lu, H. J. Zhai, S. D. Li, J. Li, and L. S. Wang (2015). *ACS Nano.* **9**, 754–760.
27. Q. Chen, S. Y. Zhang, H. Bai, W. J. Tian, T. Gao, H. R. Li, C. Q. Miao, Y. W. Mu, H. G. Lu, H. J. Zhai, and S. D. Li (2015). *Angew. Chem. Int. Ed.* **54**, 8160–8164.
28. Q. Chen, H. R. Li, C. Q. Miao, Y. J. Wang, H. G. Lu, Y. W. Mu, G. M. Ren, H. J. Zhai, and S. D. Li (2016). *Phys. Chem. Chem. Phys.* **18**, 11610–11615.
29. Q. Chen, H. R. Li, W. J. Tian, H. G. Lu, H. J. Zhai, and S. D. Li (2016). *Phys. Chem. Chem. Phys.* **18**, 14186–14190.
30. W. J. Tian, Q. Chen, H. R. Li, M. Yan, Y. W. Mu, H. G. Lu, H. J. Zhai, and S. D. Li (2016). *Phys. Chem. Chem. Phys.* **18**, 9922–9926.
31. L. Pei, H. R. Li, M. Yan, Q. Chen, Y. W. Mu, H. G. Lu, Y.-B. Wu, and S. D. Li (2018). *Phys. Chem. Chem. Phys.* **20**, 15330–15334.
32. L. Pei, M. Yan, X.-Y. Zhao, Y.-W, Mu, H.-G. Lu, Y.-B. Wu, and S.-D. Li (2020). *RSC Adv*. 10, 10129–10133.
33. H. Liu, Q. Chen, H. R. Li, X. Y. Zhao, X. X. Tian, Y. W. Mu, H. G. Lu, and S. D. Li (2018). *Phys. Chem. Chem. Phys.* **20**, 15344–15349.
34. E. Oger, N. R. M. Crawford, R. Kelting, P. Weis, M. M. Kappes, and R. Ahlrichs (2007). *Angew. Chem. Int. Ed.* **46**, 8503–8506.
35. J. Lv, Y. Wang, L. Zhu, and Y. Ma (2014). *Nanoscale* **6**, 11692–11696.
36. Y. F. Zhao, X. Chen, and J. Li (2017). *Nano Res.* **10**, 3407.
37. X. Chen, Y.-F. Zhao, L.-S. Wang, and J. Li (2017). *Comput. Theor. Chem.* **1107**, 57–65.
38. X. Chen, Y. F. Zhao, Y. Y. Zhang, and J. Li (2019). *J. Comput. Chem.* **40**, 1105.
39. X. Y. Zhao, Q. Chen, H. R. Li, Y. W. Mu, H. G. Lu, and S. D. Li (2017). *Phys. Chem. Chem. Phys.* **19**, 10998–11003.
40. C. Adamo and V. Barone (1999). *J. Chem. Phys.* **110**, 6158–6170.
41. R. Krishnan, J. S. Binkley, R. Seeger, and J. A. Pople (1980). *J. Chem. Phys.* **72**, 650–654.
42. M. J. Frisch, et al., *Gaussian 09, Revision A.2* (Gaussian Inc., Wallingford, CT, 2009).
43. J. Cizek (1969). *Adv. Chem. Phys.* **14**, 35.
44. G. D. Purvis and R. J. Bartlett (1982). *J. Chem. Phys.* **76**, 1910–1918.
45. K. Raghavachari, G. W. Trucks, J. A. Pople, and M. HeadGordon (1989). *Chem. Phys. Lett.* **157**, 479–483.
46. H. J. Werner, P. J. Knowles, G. Knizia, F. R. Manby, M. Schütz, P. Celani, T. Korona, R. Lindh, A. Mitrushenkov, et al (2012). *MOLPRO*.
47. D. Y. Zubarev and A. I. Boldyrev (2008). *Phys. Chem. Chem. Phys.* **10**, 5207–5217.
48. P. V. R. Schleyer and C. Maerker (1996). *J. Am. Chem. Soc.* **118**, 6317–6318.
49. J. VandeVondele, M. Krack, F. Mohamed, M. Parrinello, T. Chassaing, and J. Hutter (2005). *Comput. Phys. Commun.* **167**, 103–128.
50. T. T. Gao, Q. Chen, Y. W. Mu, H. G. Lu, and S. D. Li (2016). *AIP Adv.* **6**, 065110.
51. D. Ciuparu, R. F. Klie, Y. M. Zhu, and L. Pfefferle (2004). *J. Phys. Chem. B.* **108**, 3967–3969.
52. R. Bauernschmitt and R. Ahlrichs (1996). *Chem. Phys. Lett.* **256**, 454–464.